KSME

Springer

Journal of Mechanical Science and Technology 34 (6) 2020

Original Article
DOI 10.1007/s12206-020-0520-x

Keywords:
· Large-eddy simulation
· Heavy explosion
· Mushroom cloud
· Numerical methods
· Stratified flow

Correspondence to:
Changhoon Lee
clee@yonsei.ac.kr

Citation:
Won, S., Lee, C. (2020). Simulation of the mushroom cloud generated from a high-energy explosion using large-eddy simulation. Journal of Mechanical Science and Technology 34 (6) (2020) 2443~2453.
http://doi.org/10.1007/s12206-020-0520-x

Received November 5th, 2019
Revised April 2nd, 2020
Accepted April 13th, 2020

† Recommended by Editor
Yang Na

Simulation of the mushroom cloud generated from a high-energy explosion using large-eddy simulation

Sungjin Won[1] and Changhoon Lee[1,2]

[1]Department of Computational Science and Engineering, Yonsei University, Seoul 03722, Korea,
[2]Department of Mechanical Engineering, Yonsei University, Seoul 03722, Korea

Abstract We performed numerical simulations of a 20 kT heavy explosion to predict the rise and diffusion of mushroom cloud after the atmospheric pressure is recovered around the burst point. We proposed a new formulation of governing equations based on the anelastic approximation and density weighted variables to implement the atmospheric stratification by employing potential temperature to account for the effect of atmospheric pressure variation in altitude. To validate the simulation results, we chose similar explosive yield cases performed at the Nevada sites to compare the mushroom cloud height and diameter. Parametric studies were performed by varying the grid size and global subgrid-scale coefficients, C_S, to find the appropriate value that guarantees reliability of simulation results. Based on the optimal simulation results, the cooling process of mushroom cloud and the suppressed ascending air currents around tropopause were investigated.

1. Introduction

Mushroom-shaped cloud is generally observed in a high-energy explosion such as an accident in a chemical factory, power plant explosion and volcanic eruption. Generally, explosion damages the environment in the form of shock wave, thermal radiation, and dispersion of explosive debris. At the initial stage of explosion, the shock wave and thermal radiation directly hits and burns the nearby objects. After a few seconds, the mushroom cloud is generated due to buoyancy accompanied by dust and debris around the burst point. Unlike the other damages, the accompanied dusts travel a wide area and last for a long time. In addition, it can be fatal to people's health in case of any accident in a plant handling chemical, biological, or radioactive matter. Therefore, study of the generation and development of mushroom cloud would be helpful in predicting the damage from the falling harmful substances.

In general, studies related to high-energy explosions are rare or not open to the public. At the beginning of an explosion, blast wave propagation yields wide variations in density and pressure around the burst point. As density and pressure variation dominantly affect the initial phase of the explosion, it is required to use a full compressible formulation for simulation. As the early stage of explosions originates from spherical low-density hot gases, axisymmetric modeling is sufficient for investigating the effect of blast wave propagation and generation of a fireball [1]. Kanarska et al. [2] simulated flows after a few seconds of the explosion by using adaptive mesh refinement (AMR) Eulerian compressible solver [3] for calculating the compressibility dominant stage. Because the pressure around the fireball recovers the surrounding atmospheric pressure within a few seconds [1, 2], the buoyancy dominant stage can be simulated using the incompressible algorithm of Bell et al. [4], which employs projection methods based hierarchical AMR algorithm to improve the accuracy of cloud rising phenomena.

However, simulation of mushroom cloud based on the Euler equation has limited capability because it does not consider the effect of subgrid-scale (SGS) turbulence. Kim et al. [5] investigated the explosion case of Little Boy dropped in Hiroshima in 1945 by utilizing the FLUENT

solver. They validated the radius of pressure propagation with the Ref. [6] and investigated the generation process of the mushroom cloud in ambient air without the background stratification.

Present study investigates the rising of mushroom clouds using large-eddy simulation (LES) with Vreman [7] SGS model and verifies the validity of the proposed governing equations. Atmospheric stratification is considered in the governing equations to reflect the density, pressure, and temperature variations in altitude. We use the simulation data at 5 seconds after the 20 kT explosion using compressible solver from Song et al. [1] as the initial condition. Parametric studies for computational grid size and specific ranges of global SGS coefficients are tested to find the proper value by validating the simulation results with the test data from the Defense Nuclear Agency [8]. Furthermore, the cooling process of the mushroom cloud and suppressed rising air currents are investigated based on the optimal simulation results.

2. Numerical methods

The filtered governing equations are derived from three-dimensional fully compressible Navier-Stokes equation. As we are interested in the high Reynolds number phenomena, the molecular viscosity is neglected [1, 9]. As a result, the continuity and momentum equations transform as

$$\frac{\partial \rho}{\partial t}+\frac{\partial}{\partial x_j}\rho u_j=0, \tag{1}$$

$$\frac{\partial}{\partial t}\rho u_i+\frac{\partial}{\partial x_j}\rho u_i u_j=-\frac{\partial P}{\partial x_i}-\rho g\delta_{i2}, \tag{2}$$

where u_i is velocity components in i-direction, ρ is density, g is gravitational acceleration, and P is pressure. The variables, $x_1(x)$ and $x_3(z)$ denote the horizontal coordinates, and $x_2(y)$ denotes the vertical coordinate. Statistically, x_1 and x_3 are indistinguishable. To implement the background stratification, the density and temperature are decomposed as

$$\rho=\rho_b(x_2)+\rho', \tag{3}$$

$$T=T_b(x_2)+T', \tag{4}$$

where subscript b refers to vertically structured background atmospheric variables, and ρ' and T' are density and temperature fluctuations, respectively. Under the assumption of $\rho_b(x_2)\gg\rho'$ in the atmosphere, ρ is approximated as $\rho_b(x_2)$ by using the anelastic approximation except in the gravitational force term [10]. The atmospheric density $\rho_b(x_2)$ is provided from the data for US standard atmosphere, 1976 (NOAA). The standard atmospheric data are shown in Fig. 1. The anelastic approximation yields

$$\frac{\partial}{\partial x_j}\rho_b(x_2)u_j=0 \tag{5}$$

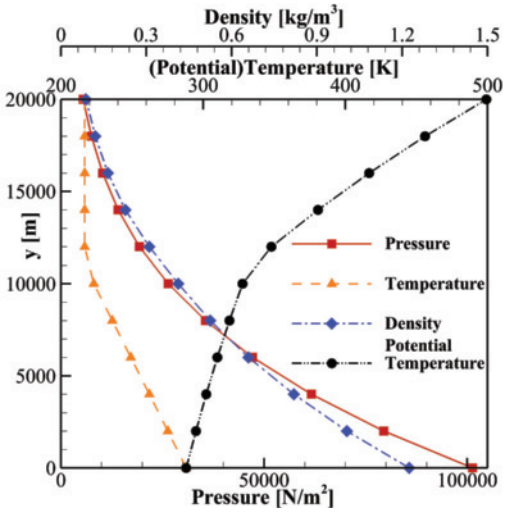

Fig. 1. Profiles of atmospheric properties based on US standard atmosphere data, 1976 (NOAA).

$$\frac{\partial}{\partial t}\rho_b(x_2)u_i+\frac{\partial}{\partial x_j}\rho_b(x_2)u_i u_j=-\frac{\partial P}{\partial x_i}-\left(\rho_b(x_2)+\rho'\right)g\delta_{i2}. \tag{6}$$

In the case of stationary fluid, for $i=2$, the atmospheric pressure gradient balances the gravitational force, $-\partial P_b(x_2)/\partial x_2=\rho_b(x_2)g$. In the right hand side of Eq. (6), the term, $-\rho_b(x_2)g\delta_{i2}$ is absorbed into the pressure gradient and the right hand side transforms into $-\partial P_D/\partial x_i+\left(\rho-\rho_b(x_2)\right)g\delta_{i2}$, where $P_D=P-P_b(x_2)$. We use the ideal gas equation to model the density, $\rho=\left(P_D+P_b(x_2)\right)/RT$, and ignore P_D in modeling the buoyancy force because the magnitude of pressure fluctuation is relatively smaller than that of the hydrostatic one ($\left|P_b(x_2)\right|\gg\left|P_D\right|$). R is the gas constant of air. Consequently, the momentum equation becomes

$$\begin{aligned}&\frac{\partial}{\partial t}\rho_b(x_2)u_i+\frac{\partial}{\partial x_j}\rho_b(x_2)u_i u_j\\&=-\frac{\partial P_D}{\partial x_i}-\frac{P_b(x_2)}{R}\left(\frac{1}{T_b(x_2)+T'}-\frac{1}{T_b(x_2)}\right)g\delta_{i2}.\end{aligned} \tag{7}$$

The next step involves filtering of variables for large-eddy simulation. The continuity and momentum equation are implicitly filtered in grid resolution by adding the residual stress term, $\tau_{ij}=\overline{u_i u_j}-\overline{u}_i\overline{u}_j$, as shown below. Overlined quantity denotes filtered quantity. As the vertical scale of the background atmospheric variables is much larger than the filter size, the background density, pressure, and temperature are not filtered.

$$\frac{\partial}{\partial x_j}\rho_b(x_2)\overline{u}_j=0, \tag{8}$$

$$\begin{aligned}&\frac{\partial}{\partial t}\rho_b(x_2)\overline{u}_i+\frac{\partial}{\partial x_j}\rho_b(x_2)\overline{u}_i\overline{u}_j\\&=-\frac{\partial \overline{P}_D}{\partial x_i}-\frac{\partial}{\partial x_j}\rho_b(x_2)\tau_{ij}-\frac{P_b(x_2)}{R}\left(\frac{1}{T_b(x_2)+\overline{T}'}-\frac{1}{T_b(x_2)}\right)g\delta_{i2}.\end{aligned} \tag{9}$$

Here, τ_{ij} is modeled using linear eddy viscosity as follows

$$\tau_{ij} = -2\nu_T \overline{S}_{ij}, \tag{10}$$

where ν_T is eddy viscosity. The filtered strain rate tensor is given by

$$\overline{S}_{ij} = \frac{\partial \overline{u}_i}{\partial x_j} + \frac{\partial \overline{u}_j}{\partial x_i}. \tag{11}$$

The dynamic Smagorinsky model [11] requires explicit filtering, ensemble averaging, and clipping process to prevent negative value of the eddy viscosity. These additional procedures increase the computational cost and can cause nontrivial effect to developing complex flows. We modeled the eddy viscosity ν_T using Vreman SGS model [7] composed of first-order derivatives of the velocity field with Smagorinsky coefficient C_S [12], which is easy to implement and performs as good as a standard dynamic model for inhomogeneous flows,

$$\nu_T = 2.5C_S^2\sqrt{B/\alpha_{ij}\alpha_{ij}}, \tag{12}$$

$$B = \beta_{ii}\beta_{jj} - \beta_{ij}^2, \tag{13}$$

$$\beta_{ij} = \sum_{m=1}^{3}\Delta_{x_m}^2\alpha_{mi}\alpha_{mj}, \tag{14}$$

$$\alpha_{ij} = \partial_i \overline{u}_j = \partial\overline{u}_j/\partial x_i, \tag{15}$$

where Δ_{x_m} denotes the x_m-directional computational grid. After accounting for the same in Eq. (9), the governing equation is obtained with modeled residual stress as

$$\begin{aligned}
&\frac{\partial}{\partial t}\rho_b(x_2)\overline{u}_i + \frac{\partial}{\partial x_j}\rho_b(x_2)\overline{u}_i\overline{u}_j = \\
&-\frac{\partial \overline{P}_D}{\partial x_i} - \frac{P_b(x_2)}{R}\left(\frac{1}{T_b(x_2)+\overline{T}'} - \frac{1}{T_b(x_2)}\right)g\delta_{i2} \\
&+\frac{\partial}{\partial x_j}\left[\nu_T\left(\frac{\partial\rho_b(x_2)\overline{u}_i}{\partial x_j} + \frac{\partial\rho_b(x_2)\overline{u}_j}{\partial x_i}\right)\right] \\
&-\frac{\partial}{\partial x_j}\left[\nu_T\left(\overline{u}_i\frac{\partial\rho_b(x_2)}{\partial x_j} + \overline{u}_j\frac{\partial\rho_b(x_2)}{\partial x_i}\right)\right].
\end{aligned} \tag{16}$$

As the atmospheric density variations in the vertical direction yield stratification effect, it needs to be taken into consideration in solving the equation. To this end, the background-density weighted velocity is introduced,

$$\tilde{u}_i = \rho_b(x_2)u_i/\rho_0, \tag{17}$$

where ρ_0 is ground air density. Then the continuity and Navier-Stokes equations are finally transformed to

$$\frac{\partial}{\partial x_j}\tilde{\overline{u}}_j = 0, \tag{18}$$

$$\begin{aligned}
&\frac{\partial}{\partial t}\tilde{\overline{u}}_i + \frac{\partial}{\partial x_j}\frac{\rho_0}{\rho_b(x_2)}\tilde{\overline{u}}_i\tilde{\overline{u}}_j = \\
&-\frac{1}{\rho_0}\frac{\partial\overline{P}_D}{\partial x_i} + \frac{\partial}{\partial x_j}\left[\nu_T\left(\frac{\partial\tilde{\overline{u}}_i}{\partial x_j} + \frac{\partial\tilde{\overline{u}}_j}{\partial x_i}\right)\right] \\
&-\frac{P_b(x_2)}{\rho_0 R}\left(\frac{1}{T_b(x_2)+\overline{T}'} - \frac{1}{T_b(x_2)}\right)g\delta_{i2} \\
&-\frac{1}{\rho_0}\frac{\partial}{\partial x_j}\left[\nu_T\left(\overline{u}_i\frac{\partial\rho_b(x_2)}{\partial x_j} + \overline{u}_j\frac{\partial\rho_b(x_2)}{\partial x_i}\right)\right].
\end{aligned} \tag{19}$$

The atmospheric variables change in altitude as shown in Fig. 1, the rarefied high-altitude air shows much lower pressure and density than the ground values. Temperature profile shows inversion in low altitude, but potential temperature profile clearly shows that the atmosphere is stably stratified. To derive the thermal energy equation in this stratified situation, we introduce potential temperature, θ, defined as follows.

$$\theta = T\left(\frac{p_0}{p}\right)^{R/c_P}, \tag{20}$$

where c_p is the specific heat capacity of air at a constant pressure. Beginning with the isentropic assumption,

$$ds = c_p\frac{dT}{T} - R\frac{dP}{P} = \frac{c_p}{T}\left(\frac{P}{P_0}\right)^{R/c_p}d\theta = 0. \tag{21}$$

We could see that the potential temperature is advectively conserved, suggesting

$$\frac{D\theta}{Dt} = 0, \tag{22}$$

or, using the density-weighted variables,

$$\frac{\partial\theta}{\partial t} + u_j\frac{\partial\theta}{\partial x_j} = 0, \tag{23}$$

$$\frac{\partial\theta}{\partial t} + \frac{\rho_0}{\rho_b(x_2)}\tilde{u}_j\frac{\partial\theta}{\partial x_j} = 0, \tag{24}$$

$$\frac{\partial\theta}{\partial t} + \frac{\partial}{\partial x_j}\left(\frac{\rho_0}{\rho_b(x_2)}\tilde{u}_j\theta\right) - \theta\frac{\rho_0}{\rho_b(x_2)}\frac{\partial\tilde{u}_j}{\partial x_j} - \tilde{u}_2\theta\frac{d}{dx_2}\left(\frac{\rho_0}{\rho_b(x_2)}\right) = 0. \tag{25}$$

Here, $\partial\tilde{u}_j/\partial x_j$ can be put to zero due to continuity equation from Eq. (5). Then, the modified Eq. (23) is given by

$$\frac{\partial\theta}{\partial t} + \frac{\partial}{\partial x_j}u_j\theta - \frac{\rho_b(x_2)}{\rho_0}u_2\theta\frac{d}{dx_2}\left(\frac{\rho_0}{\rho_b(x_2)}\right) = 0, \tag{26}$$

where u_2 is the vertical velocity in y-direction. The govern-

for all control volumes V_i **do**
  $\theta^n \xrightarrow{\text{QUICK}} \theta^*$
end for
for all control volumes V_i **do**
  if $\theta^* > \theta_{max}$ or $\theta^* < \theta_{min}$ **then**
    $\theta^{n+1}(x_i) = \theta^n(x_i - u_i^{n+1}\Delta t)$
  else
    $\theta^{n+1}(x_i) = \theta^*$
  end if
end for

Fig. 2. Algorithm of the IBQUICK scheme.

ing equation is then implicitly filtered in grid resolution to yield the residual flux term, $q_j = \overline{u_j\theta} - \overline{u}_j\overline{\theta}$.

$$\frac{\partial\overline{\theta}}{\partial t} + \frac{\partial}{\partial x_j}\overline{u}_j\overline{\theta} - \frac{\rho_b(x_2)}{\rho_0}\overline{u}_2\overline{\theta}\frac{d}{dx_2}\left(\frac{\rho_0}{\rho_b(x_2)}\right) = -\frac{\partial q_j}{\partial x_j} + \frac{\rho_b(x_2)}{\rho_0}q_2\frac{d}{dx_2}\left(\frac{\rho_0}{\rho_b(x_2)}\right) \tag{27}$$

Here, q_j is modeled by linear eddy diffusivity as follows

$$q_j = -\alpha_T\frac{\partial\overline{\theta}}{\partial x_j} \tag{28}$$

where α_T is the eddy diffusivity, which is defined as

$$\alpha_T = \frac{\nu_T}{Pr_T}, \tag{29}$$

where Pr_T is the turbulent Prandtl number, which is set to 1.0 in the current study. The filtered governing equation with the modeled residual term is given by

$$\frac{\partial\overline{\theta}}{\partial t} + \frac{\partial}{\partial x_j}\overline{u}_j\overline{\theta} = \frac{\partial}{\partial x_j}\left(\alpha_T\frac{\partial\overline{\theta}}{\partial x_j}\right) + \frac{\rho_b(x_2)}{\rho_0}\overline{u}_2\overline{\theta}\frac{d}{dx_2}\left(\frac{\rho_0}{\rho_b(x_2)}\right) - \frac{\rho_b(x_2)}{\rho_0}\alpha_T\frac{\partial\overline{\theta}}{\partial x_2}\frac{d}{dx_2}\left(\frac{\rho_0}{\rho_b(x_2)}\right). \tag{30}$$

Further, we substitute the velocity variables into the density-weighted variables. Then the final form of the energy equation obtained is given by

$$\frac{\partial\overline{\theta}}{\partial t} + \frac{\partial}{\partial x_j}\left(\frac{\rho_0}{\rho_b(x_2)}\widetilde{\overline{u}}_j\overline{\theta}\right) = \frac{\partial}{\partial x_j}\left(\alpha_T\frac{\partial\overline{\theta}}{\partial x_j}\right) + \widetilde{\overline{u}}_2\overline{\theta}\frac{d}{dx_2}\left(\frac{\rho_0}{\rho_b(x_2)}\right) - \frac{\rho_b(x_2)}{\rho_0}\alpha_T\frac{\partial\overline{\theta}}{\partial x_2}\frac{d}{dx_2}\left(\frac{\rho_0}{\rho_b(x_2)}\right). \tag{31}$$

The governing equations are solved using a third-order hybrid Runge-Kutta time integration scheme [13] and the second-order central difference spatial discretization scheme with flux correction method. Conventional flux correction method improves stability and accuracy of the central difference scheme to solve a scalar transport equation [14]. Especially, the bounded QUICK (BQUICK) scheme [15] corrects variables found in an unexpected range by using a one-dimensional upwind scheme. However, BQUICK scheme is not appropriate for replacing faulty data in the current simulation, because it does not consider the size of the grid and the magnitude of velocity. Since temperature sharply varies with the grid in the present simulation, we need to take the grid size and the velocity magnitude into consideration.

Therefore, interpolative BQUICK (IBQUICK) scheme is proposed for the estimation of the scalar value. The modified method works when the updated variable violates the physical boundedness of the scalar. In the correction process, the next step data in the subsequent step, θ^{n+1}, is replaced by the present data at the updated position. Since the position usually does not coincide with the grid points, we interpolate the scalar variable at the expected position. The detailed algorithm is explained in Fig. 2.

Flow driven by buoyancy force is critically affected by temperature of the flow field. To obtain accurate simulation results, we need to use as accurate an initial temperature data as possible. Heavy explosion shows unpredictable temperature distribution within a fireball. Therefore, for the initial condition, we used the simulation data from Song et al. [1], which was estimated using compressible Navier-Stokes solver. Based on Song's data, we extracted the temperature and the velocity fields after 5 seconds of the 20 kT heavy explosion when the pressure field almost recovers the atmospheric pressure. Fig. 3 shows the temperature contour within the fireball. As this field is structured as a two-dimensional axisymmetric data, we rotated the data in the cylindrical coordinates and converted it into Cartesian coordinates to use it as an initial condition. We verified that Song et al. [1]'s initial condition contains 20 kT energy amount. Additionally, we confirmed that the energy amount at 5 seconds after explosion in Song et al. [1]'s simulation result is properly reflected in the present initial condition. Further, mean-zero random fluctuations were added to the initial field to break symmetricity of the flow field. At the bottom of the domain, no-slip boundary condition was imposed while the slip boundary condition was specified at the top. Horizontally, the periodic boundary condition was imposed using the FFTW library [16]. Computational grid was uniformly distributed in all directions. As the maximum height of the mushroom cloud is predicted to be around 10 km within the first 4 minutes, we set the vertical domain size and the horizontal domain size as 20 km and 10 km, respectively.

3. Reference considered for validation

We referred to the explosion test data from Defense Nuclear Agency [8] to validate our simulation results. The test data were organized into a variety of explosion cases categorized with respect to the operation name, explosive yield, burst

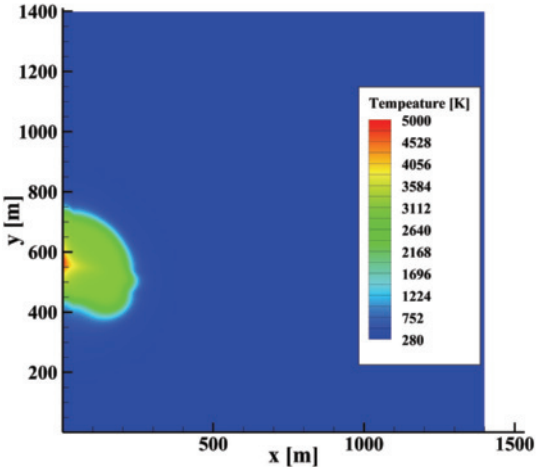

Fig. 3. Temperature contour of two-dimensional axisymmetric simulation after 5 seconds of the 20 kT explosion [1].

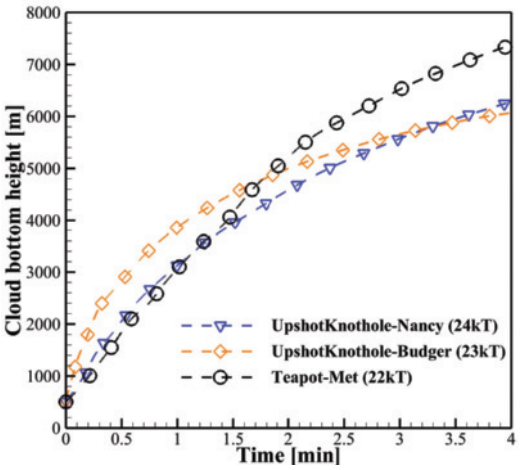

Fig. 5. Time histories of cloud bottom height observation data measured ±20 % around the 20 kT explosion.

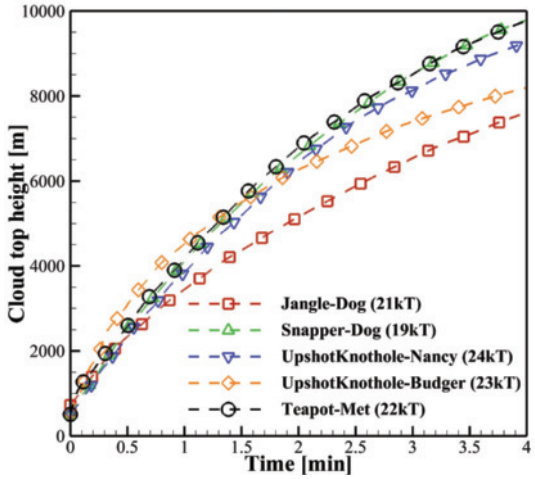

Fig. 4. Time histories of cloud top height observation data measured ±20 % around the 20 kT explosion.

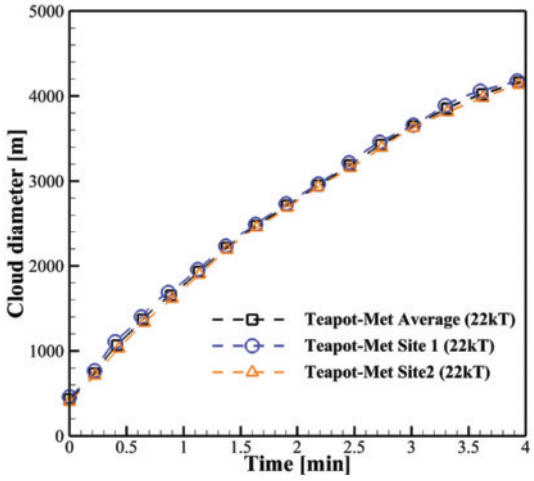

Fig. 6. Time histories of cloud diameter observation data measured ±20 % around the 20 kT explosion.

height, burst type and placement, etc., which were carried out at the Nevada sites. We selected ten test cases that satisfy the criteria of 20 kT ± 20 % explosion yield, and five test cases of them containing the dimensional data of the mushroom cloud were finally chosen. Because all the explosions were tested in different initial conditions, the ascension rate and shape of the mushroom cloud are non-equivalent. To compare our simulation results with the data, we equalized the site elevation and height of the burst to the reference. The interpolated graphs are plotted in Figs. 4-6. To validate the present simulation results, the range of the top, bottom, and diameter of the mushroom cloud from 5 test data are compared.

4. Results

The initial data obtained from the simulation by Song et al. [1] were converted to the coordinate system of the present simulation. Table 1 lists the simulation parameters for grid comparison test and Fig. 7 depicts the horizontal distribution of the initial temperature field at an altitude of 550 m from the ground. 6 points in A1, 8 points in A2, 9 points in A3, and 11 points in A4 are uniformly distributed in the radial direction within the high temperature region $(0\ \mathrm{m} \le x \le 300\ \mathrm{m})$. Depending on the grid sizes, data insufficiency in steep gradient region $(200\ \mathrm{m} \le x \le 250\ \mathrm{m})$ and underestimated local maximum temperature are observed.

To verify the results in detail, we compared the simulation data of the top, bottom and diameter of the mushroom cloud with the reference at an interval of 30 seconds in Fig. 8. In the real situation, bulk of dust and condensed vapor of the air are fed into the rising core area along with the turbulent vortex ring around the edge, which is recognized as a mushroom cloud. As dust particles and the condensation of vapor in the air are not considered, the shape of the mushroom cloud is presumed based on the potential temperature fluctuation, $\theta' = \theta - \theta_b(y)$. Comparison of the cloud dimensions for different grid resolutions shown in Fig. 8 clearly shows that as the grid size decreases, all cloud dimensions tend to converge. Simulations

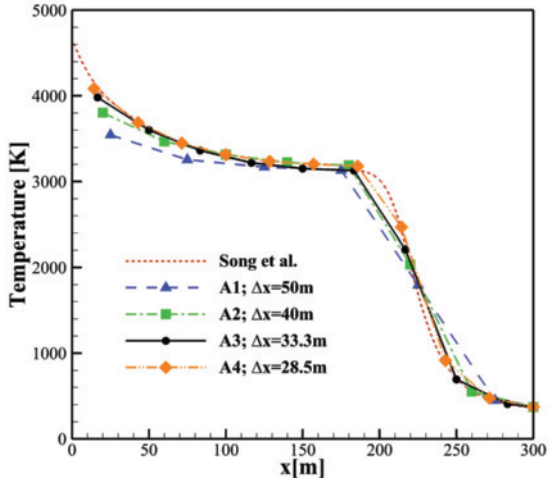

Fig. 7. Comparison of initial temperature distribution measured at 550 m height; red dashed line: Song et al. [1], blue dashed line with triangle symbol: $\Delta_x = 50.0$ m, green dash-dot line with square symbol: $\Delta_x = 40.0$ m, black solid line with circle symbol: $\Delta_x = 33.3$ m, orange dash-dot-dot line with diamond symbol: $\Delta_x = 33.3$ m.

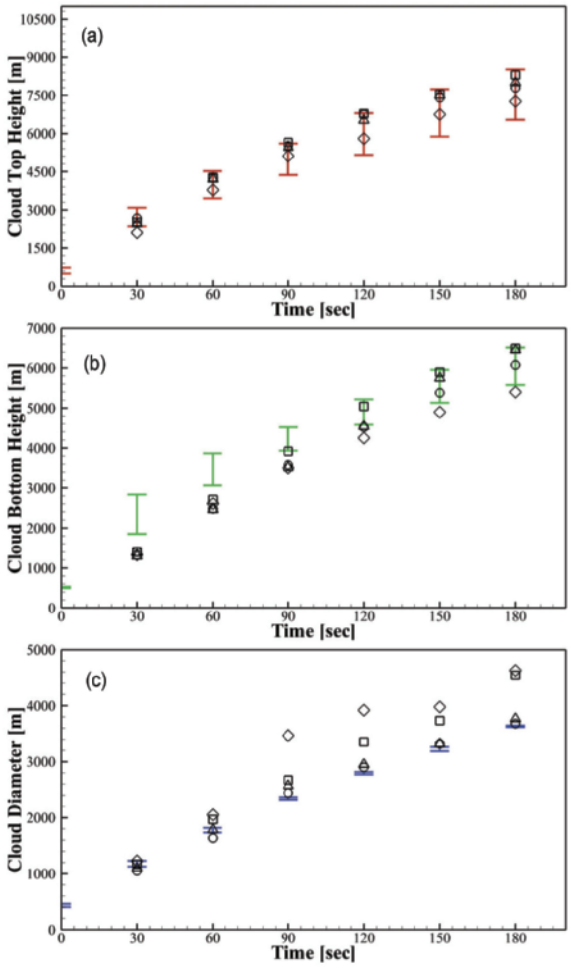

Fig. 8. Cloud: (a) Top height; (b) bottom height; (c) diameter comparison data in different grid sizes measured at an interval of 30 seconds; ◇: $\Delta_x = 50.0$ m, □: $\Delta_x = 40.0$ m, △: $\Delta_x = 33.3$ m, ○: $\Delta_x = 28.5$ m, error bar: experimental data from defense nuclear agency [8].

Table 1. Simulation parameters for grid comparison test.

Case	N_x	N_y	N_z	$\Delta_{x,y,z}$	C_S
A1	201	401	201	50.0 m	0.12
A2	251	501	251	40.0 m	
A3	301	601	301	33.3 m	
A4	351	701	351	28.5 m	

Table 2. Simulation parameters for SGS coefficient comparison test.

Case	N_x	N_y	N_z	$\Delta_{x,y,z}$	C_S
B1	301	601	301	33.3 m	0.08
B2					0.10
B3					0.12
B4					0.15
B5					0.20

with coarse grids (cases A1 and A2) yield underestimated cloud bottom height and overestimated cloud diameter. Overall, cases A3 and A4 show convergence with good agreement with the observed data. Since the grid of case A3 is sufficient as a threshold value, it is used as a standard resolution in present simulation.

As the globally constant SGS coefficient can yield excessive or weak suppression of turbulence in the entire computational domain, an appropriate choice of the value of C_s is required for good prediction. In commercial software, the value of C_s around 0.1 has been frequently used to yield better results for various types of flow. Therefore, we tested five different values of C_s around 0.1 to find the appropriate value that can yield the best validation. Table 2 summarizes the simulation parameters of SGS coefficient comparison test. In Fig. 9, the overall simulation results show a certain trend with variation in C_s values. As C_s directly affects the magnitude of diffusion, the influence of convection can be emphasized or weakened by changing the SGS coefficient. The high temperature gases vigorously rise in the core of the explosion because of the buoyancy force and the initial fast vertical velocity generated by the reflected blast wave from the ground. In this physical phenomenon, the ascending momentum of gases is dominantly affected by convective terms of the equation. In Fig. 9, rapid rise of high-temperature gases in the core of explosion is forming a vertically sharp head of mushroom cloud under for $C_s = 0.12$. Because of the fast-rising air in the central region, the shape of the cloud resembles a stratified double mushroom cloud. On the other hand, suppressed rising mushroom cloud with excessive diffusion is observed for larger values of C_s. For moderate range of C_s, the balanced convection and diffusion shows that the ascending air current gets mingled with the turbulent vortex around the edge.

In Fig. 10, dimensional parameters of the simulated mushroom cloud are plotted at an interval of 30 seconds. From the data, cloud top height shows good agreement with the

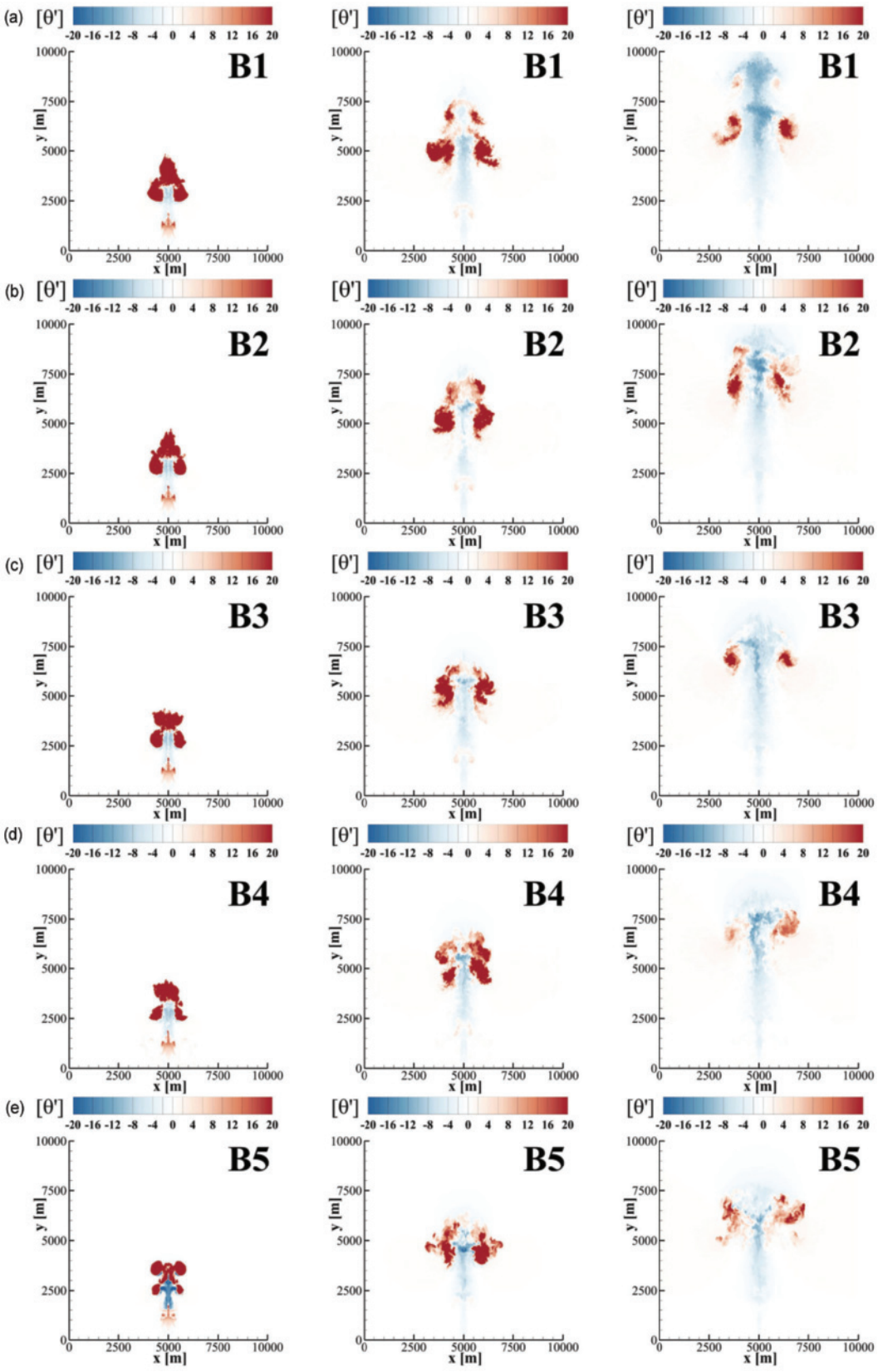

Fig. 9. Potential temperature fluctuation contours for different global SGS coefficients at 60, 120, and 180 seconds: (a) $C_s = 0.08$; (b) $C_s = 0.10$; (c) $C_s = 0.12$; (d) $C_s = 0.15$; (e) $C_s = 0.20$.

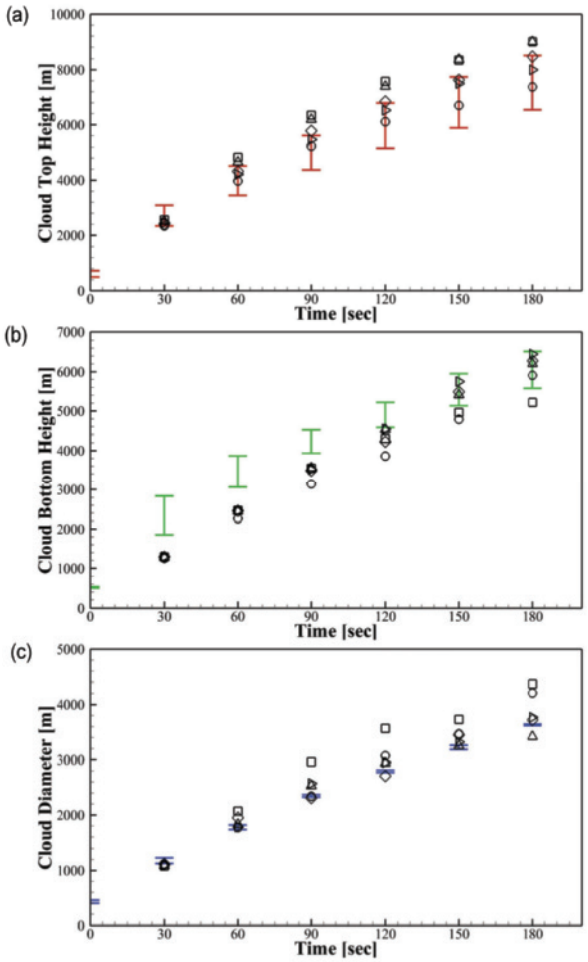

Fig. 10. Cloud: (a) Top height; (b) bottom height; (c) diameter comparison data in different SGS coefficient measured at an interval of 30 seconds; □: $C_s = 0.08$, △: $C_s = 0.10$, ▷: $C_s = 0.12$, ◇: $C_s = 0.15$, ○: $C_s = 0.20$, error bar: Test data from Defense Nuclear Agency [8].

reference over $C_s = 0.12$, while overall cloud bottom height is underestimated until 90 seconds. As lower region ascends, the bottom height for $C_s = 0.10$~0.15 shows good agreement with the reference after 120 seconds. Diameter of mushroom cloud strongly depends on the variation of SGS coefficient. As mentioned above, large SGS coefficient emphasizes the momentum diffusion and relatively weakens the convection, and it results in the over predicted value of the cloud diameter for $C_s = 0.20$. For $C_s = 0.08$, on the other hand, fast rising air current thrusts the ascending high temperature turbulent vortex away, thus the cloud diameter is expected to be larger than the reference data. From the investigation of cloud dispersion, it is recommended to select the value of C_s between 0.10 and 0.15. As the SGS coefficient of 0.12 shows the highest accuracy in top, bottom, and diameter, we choose 0.12 as the appropriate C_S value in this simulation.

The high-energy explosion initially yields blast waves and heat radiation. The propagated blast wave is reflected from the ground and distorts the shape of fireball with pressure recovering around the burst point. After this stage, the rising mushroom cloud is developed due to strong buoyancy force. Based on the present simulation, the maximum temperature of the initial stage is about 4.0×10^3 K at 5 seconds after the explosion, so the lowest density of the fireball is about 1/15 of that of the ambient air.

The density difference between fluids causes the Rayleigh-Taylor instability that yields turbulence, and the rising mushroom cloud is developed with a vortex ring around the edge of the fireball. A few minutes after the explosion, the vigorously rising mushroom cloud gradually loses its vertical and rotational momentum and temperature as shown in Figs. 11 and 12.

As the rising vortex ring loses its own temperature by expanding itself in the rarified air and sucks the ambient air into its center, the temperature difference between the mushroom

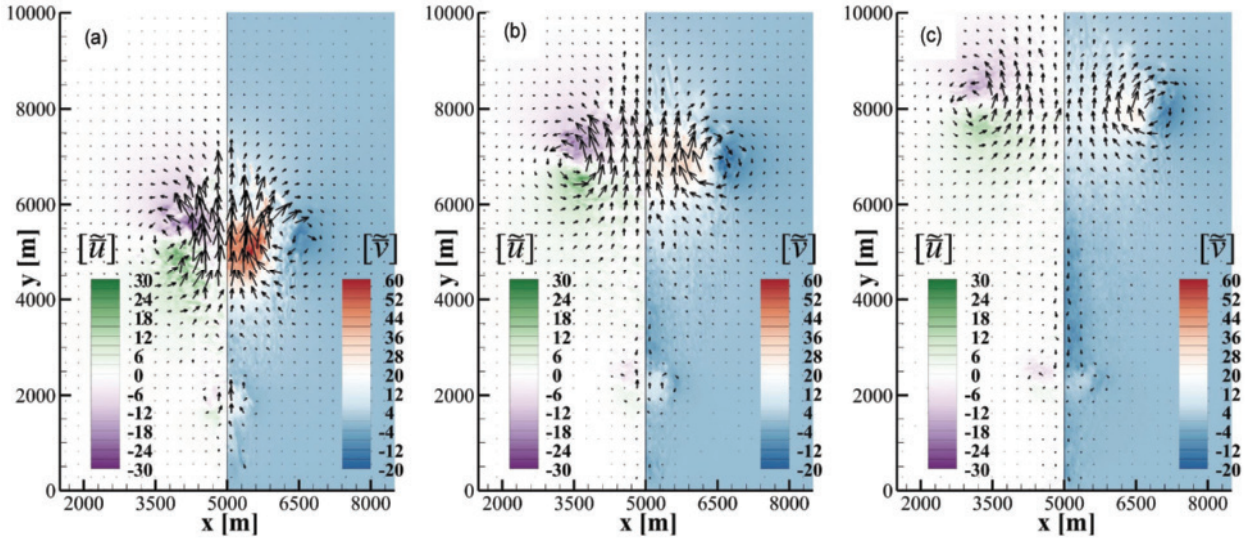

Fig. 11. Time evolution of the density-weighted filtered (left) horizontal velocity and (right) vertical velocity with the vector of the mushroom cloud at (a) 120 seconds; (b) 180 seconds; (c) 240 seconds.

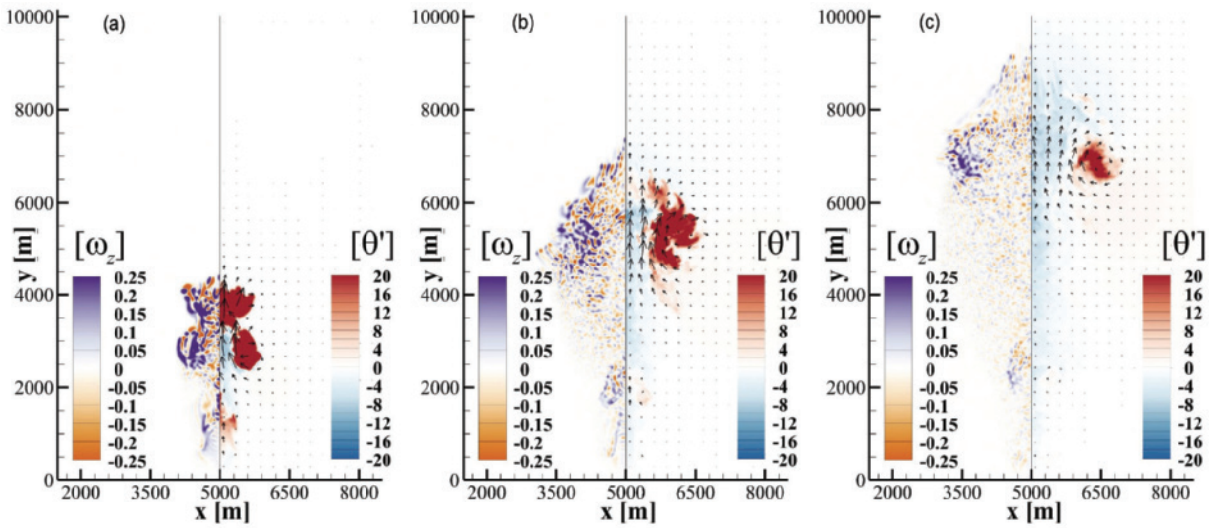

Fig. 12. Time evolution of (left) vorticity and (right) potential temperature fluctuations with the vector of the mushroom cloud at (a) 60 seconds; (b) 120 seconds; (c) 180 seconds.

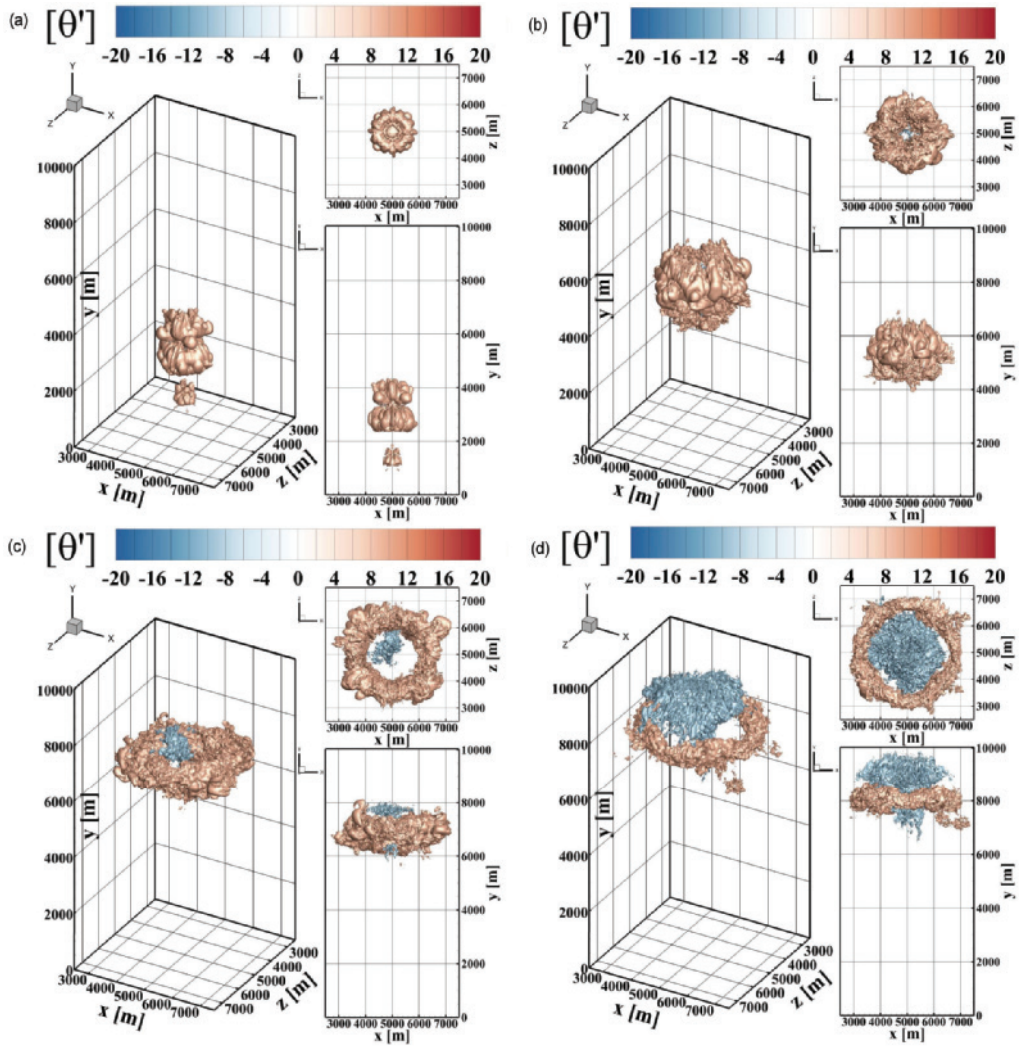

Fig. 13. Three-dimensional iso-surface contour for $C_s = 0.12$, $\theta' = 10K$, and $-10K$ at (a) 60 seconds; (b) 120 seconds; (c) 180 seconds; (d) 240 seconds.

cloud and the high-altitude atmosphere shows little difference, which mitigates the buoyancy force [17]. If the atmospheric potential temperature were neutrally or unstably stratified, the rising momentum would last longer because it would keep the temperature difference even at the high altitudes. Due to the atmospheric stratification, the rising high temperature gases are naturally suppressed during ascension, especially around the tropopause.

The velocity contours in Fig. 11 show gradually suppressed rising mushroom cloud sustaining the Rayleigh-Taylor instability until 240 seconds after the explosion. From the vector distribution shown in Figs. 11 and 12, the formation of the Rayleigh-Taylor instability around the edge of mushroom cloud consistently draws the outer air into the core region.

As shown in Figs. 12 and 13, the hot gases that rotate in toroidal shape retain their shape for a quite long time, while the core region is rapidly cooled by the cold air entrained from the outside. Since the atmospheric potential temperature is stably stratified, the cold air from bottom region is drawn upwards with the afterwinds. Consequently, the overall processes related to atmospheric stratification such as expansion of the ascending air, and cooling of the mushroom cloud due to turbulent vortex ring causes energy loss of the cloud in strong diffusion processes around the tropopause.

5. Conclusions

In this study, we proposed a three-dimensional incompressible flow solver for predicting the motion of a mushroom cloud after a 20 kT explosion in the stratified atmosphere. The incompressible filtered governing equations using Vreman SGS model [7] were derived from the fully compressible Navier-Stokes equations and the isentropic approximation. Under the assumption of small density and pressure fluctuations, anelastic approximation was used and density weighted average transformed the governing equations into an incompressible form. The energy equation was derived based on the potential temperature that reflects the pressure ratio of the atmosphere. For the accurate simulations of the energy equation, an improved flux correction method was suggested to overcome the limitation of the traditional upwinding scheme. The equations were discretized by using the 2nd order central difference method in space and the hybrid 3rd order Runge-Kutta method in time.

To validate the simulation results at every 30 seconds, we referred to experimental data of 20 kT ± 20 % explosions [8] for the shape of the mushroom cloud. Parametric studies for grid, and global SGS coefficient were performed to obtain correct simulation data. A wide range of the SGS global model constant was tested to find the appropriate value to be between 0.05 and 0.20. Since the model constant is directly related to the magnitude of diffusion, a low value of C_s enforces the role of convective momentum and ascending air current. On the other hand, large value of C_s enforces the role of diffusive momentum; hence, the rising mushroom cloud is vertically suppressed and horizontally diffused. Excessive suppression or rapid ascent of mushroom clouds yielded over predicted diameter and cloud height beyond the range of reference data. Based on the numerical verification, $C_s = 0.12$, showed good agreement with experimental data. Flow characteristics of the mushroom cloud were investigated based on the optimal simulation results. The velocity contours in horizontal and vertical directions showed sustainability of toroidal shape until 240 seconds after the explosion. Vigorously ascending air current was suppressed around the tropopause and the cloud started to diffuse, simultaneously. As the rotating turbulent vortex drew outer cold air into the hot core region, density difference between the mushroom cloud and the atmosphere gradually decreased. This phenomenon induced loss in buoyancy force and the eventual cessation of the rise of the mushroom cloud.

Acknowledgments

This research was supported by ADD (No. 17-113-601-026).

Nomenclature

C_s : Smagorinsky SGS coefficient
c_p : Specific heat capacity
f_i : Body force
g : Gravitational acceleration
L_x : Domain size in x direction
N_x : Grid number in x direction
P : Pressure
P_b : Atmospheric pressure in altitude
P_D : Hydrodynamic pressure
P_0 : Ground air pressure
q_j : Residual flux
R : Gas constant of air
s : Entropy
T : Temperature
T_b : Atmospheric temperature in altitude
T' : Temperature fluctuation
u_j : Velocity in j direction
$\bar{X}$: Filtered variable
$\tilde{X}$: Density-weighted variable
α_T : Eddy diffusivity
β : Thermal expansion coefficient
θ : Potential temperature
θ_b : Atmospheric potential temperature in altitude
θ' : Potential temperature fluctuation
ν_T : Eddy viscosity
ρ : Density
ρ_b : Atmospheric density in altitude
ρ_0 : Ground air density
ρ' : Density fluctuation
τ_{ij} : Residual shear stress

References

[1] S. Song, Y. Li, C. Lee and J. Choi, Effect of surface conditions

on blast wave propagation, *Journal of Mechanical Science and Technology*, 30 (9) (2016) 3907-3915.
[2] Y. Kanarska, I. Lomov, L. Glenn and T. Antoun, Numerical simulation of cloud rise phenomena associated with nuclear bursts, *Annals of Nuclear Energy*, 36 (2009) 1475-1483.
[3] I. Lomov, Simulation of dense and dilute multiphase compressible flows with Eulerian-Lagrangian approach, *Proc. of 6th international Conference on Multiphase Flow*, Leipzig, Germany (2007).
[4] J. B. Bell, M. S. Day, C. A. Rendleman, S. E. Woosley and M. Ingale, Adaptive low Mach number modeling of nuclear flame microphysics, *Journal of Computational Physics*, 195 (2003) 677-694.
[5] J. Kim, S. Kim, J. Choi and W. Sim, Simulation of blast wave propagation and mushroom cloud formation by a bomb explosion, *55th AIAA Aerospace Sciences Meeting and Exhibit Journal*, Grapevine, Texas, USA (2017).
[6] S. Glasstone and P. J. Dolan, *The Effects of Nuclear Weapons*, US DoD (1977).
[7] A. W. Vreman, An eddy-viscosity subgrid-scale model for turbulent shear flow: Algebraic theory and applications, *Physics of Fluids*, 16 (10) (2004) 3670-3681.
[8] H. A. Hawthrone, *Compilation of Local Fallout Data from Test Detonations 1945-1962 Extracted from DASA 1251 Volume I - Continental U.S. Tests*, Defense Nuclear Agency, Washington, D.C, USA (1979).
[9] P. Bauweraerts and J. Meyers, On the feasibility of using large-eddy simulations for real-time turbulent-flow forecasting in the atmospheric boundary layer, *Boundary-Layer Meteorology*, 171 (2019) 213-235.
[10] B. J. Hoskins and I. N. James, *Fluid Dynamics of the Mid-Latitude Atmosphere*, John Wiley & Sons, Ltd. UK (2014).
[11] M. Germano, U. Piomelli, P. Moin and W. H. Cabot, A dynamic subgrid-scale eddy-viscosity model, *Physics of Fluids A*, 3 (1991) 1760-1765.
[12] J. Smagorinsky, General circulation experiments with the primitive equations, *Monthly Weather Review*, 91 (3) (1963) 99-164.
[13] M. M. Rai and P. Moin, Direct simulations of turbulent flow using finite-difference schemes, *Journal of Computational Physics*, 96 (1991) 15-53.
[14] B. P. Leonard, A stable and accurate convective modelling procedure based on quadratic upstream interpolation, *Computer Methods in Applied Mechanics and Engineering*, 19 (1979) 59-98.
[15] M. Hermann and G. Blanquart, Flux corrected finite volume scheme for preserving scalar boundedness in reacting large-eddy simulations, *43rd AIAA Aerospace Sciences Meeting and Exhibit Journal*, Reno, Nevada, USA (2005).
[16] M. Frigo and S. G. Johnson, The design and implementation of FFTW3, *Proc. of IEEE*, 93 (2) (2005) 216-231.
[17] R. J. Ritter, *The Newsletter for America's Atomic Veterans*, National Association of Atomic Veterans, Inc., July (2013).

Sungjin Won received his B.S. (2014) from Yonsei University, Seoul, Korea in Mechanical Engineering. He is an integrated Ph.D. student in the Department of Computational Science & Engineering, Yonsei University, Korea. His research interests include large-eddy simulation, immersed boundary methods, and in the area of incompressible fluid dynamics.

Changhoon Lee received his B.S. (1985) and M.S. (1987) from Seoul National University, Seoul, Korea and Ph.D. (1993) from UC Berkeley, USA in Mechanical Engineering. He is a Professor in the Department of Computational Science & Engineering and Department of Mechanical Engineering, Yonsei University, Korea. His research interests include fundamentals of turbulence, particle-turbulence interaction, numerical algorithms, air pollution modeling and stochastic processes.